# Low-mass dark matter search results from full exposure of the PandaX-I experiment

Xiang Xiao,[1] Xun Chen,[1] Andi Tan,[7] Yunhua Chen,[8] Xiangyi Cui,[1] Deqing Fang,[4] Changbo Fu,[1] Karl L. Giboni,[1] Haowei Gong,[1] Guodong Guo,[1] Ming He,[1] Xiangdong Ji,[1,6,7,*] Yonglin Ju,[2] Siao Lei,[1] Shaoli Li,[1] Qing Lin,[1,‡] Huaxuan Liu,[2] Jianglai Liu,[1] Xiang Liu,[1] Wolfgang Lorenzon,[5] Yugang Ma,[4] Yajun Mao,[6] Kaixuan Ni,[1] Kirill Pushkin,[1,5] Xiangxiang Ren,[3] Michael Schubnell,[5] Manbin Shen,[8] Yuji Shi,[1] Scott Stephenson,[5] Hongwei Wang,[4] Jiming Wang,[8] Meng Wang,[3] Siguang Wang,[6] Xuming Wang,[1] Zhou Wang,[2] Shiyong Wu,[8] Mengjiao Xiao,[1,†] Pengwei Xie,[1] Binbin Yan,[3] Yinghui You,[8] Xionghui Zeng,[8] Tao Zhang,[1] Li Zhao,[1] Xiaopeng Zhou,[6] and Zhonghua Zhu[8]

(PandaX Collaboration)

[1]*INPAC and Department of Physics and Astronomy, Shanghai Jiao Tong University, Shanghai Laboratory for Particle Physics and Cosmology, Shanghai 200240, People's Republic of China*
[2]*School of Mechanical Engineering, Shanghai Jiao Tong University, Shanghai 200240, People's Republic of China*
[3]*School of Physics and Key Laboratory of Particle Physics and Particle Irradiation (MOE), Shandong University, Jinan 250100, China*
[4]*Shanghai Institute of Applied Physics, Chinese Academy of Sciences, Shanghai 201800, People's Republic of China*
[5]*Department of Physics, University of Michigan, Ann Arbor, Michigan 48109, USA*
[6]*School of Physics, Peking University, Beijing 100080, People's Republic of China*
[7]*Department of Physics, University of Maryland, College Park, Maryland 20742, USA*
[8]*Yalong River Hydropower Development Company, Ltd., 288 Shuanglin Road, Chengdu 610051, People's Republic of China*

(Received 10 May 2015; published 15 September 2015)

We report the results of a weakly interacting massive particle (WIMP) dark matter search using the full 80.1 live-day exposure of the first stage of the PandaX experiment (PandaX-I) located in the China Jin-Ping Underground Laboratory. The PandaX-I detector has been optimized for detecting low-mass WIMPs, achieving a photon detection efficiency of 9.6%. With a fiducial liquid xenon target mass of 54.0 kg, no significant excess events were found above the expected background. A profile likelihood ratio analysis confirms our earlier finding that the PandaX-I data disfavor all positive low-mass WIMP signals reported in the literature under standard assumptions. A stringent bound on a low-mass WIMP is set at a WIMP mass below 10 GeV/$c^2$, demonstrating that liquid xenon detectors can be competitive for low-mass WIMP searches.

DOI: 10.1103/PhysRevD.92.052004 PACS numbers: 95.35.+d, 29.40.-n, 95.55.Vj

## I. INTRODUCTION

The existence of gravitationally attractive "dark matter" that dominates the matter composition of the Universe has been firmly established based on overwhelming evidence from astronomical and cosmological observations [1]. Whether such abundant matter consists of yet unknown elementary particles remains one of the most pressing scientific questions. There are strong theoretical motivations for the existence of beyond the Standard Model physics, many of which naturally predict new stable neutral particles at the electroweak symmetry-breaking scale with weak interactions, generically named weakly interacting massive particles (WIMPs) [2,3]. WIMPs are a leading dark matter (DM) candidate where weak interactions between WIMPs and ordinary matter allow for a direct search for these particles through particle physics experiments. In recent decades, direct searches of WIMP interactions with terrestrial detectors have been carried out in deep underground laboratories worldwide with ever increasing discovery power [4].

Since 2008, a number of underground direct-detection experiments have reported signals that could be interpreted as WIMP interactions within the detector. Among those are the DAMA/LIBRA experiment using NaI(Tl) crystals [5], the CoGeNT experiment [6] using point-contact Ge detectors, the CRESST-II experiment [7] using cryogenic $CaWO_4$ bolometers (excess not reproduced in the recent

[*]PandaX Collaboration Spokesperson.
xdji@sjtu.edu.cn, xji@umd.edu
[†]Corresponding author.
xiaomengjiao@sjtu.edu.cn
[‡]Corresponding author.
mcfate@sjtu.edu.cn

 

experiment [8]), as well as the CDMS-Si experiment using cryogenic Si bolometers [9]. Although the claimed signals are not generically consistent, they all point to low to median WIMP mass in the range of 10 to 50 GeV/$c^2$. On the other hand, the ZEPLIN-III [10], XENON-100 [11], LUX [12], and PandaX-I [13] experiments utilizing xenon, the DarkSide-50 experiment using argon [14], the SuperCDMS [15,16] and CDEX [17] experiments using Ge as targets, as well as the KIMS experiment [18] using CsI(Tl) crystals, are in disagreement with some or all of these claims.

To achieve sensitivities to WIMPs beyond the current experimental bounds, detectors with larger targets, lower background, and lower energy threshold are required. In the past decade, dual-phase xenon detectors have rapidly emerged as one of the most promising technologies in WIMP direct detection, leading the WIMP search sensitivity in a wide range of parameter space [10–12,19], demonstrating superior scalability in mass, and the capability to shield against and reject background. However, in comparison to the cryogenic bolometers [8,15] or semiconductor ionization detectors [6,16,17], dual-phase liquid xenon detectors have not demonstrated the ability to obtain a comparably low energy threshold. Conventionally, the issue is attributed to insufficient light collection efficiency or a lack of understanding of the low-energy nuclear recoil (NR) quenching factor. In recent years, the LUX and PandaX collaborations operated newly designed liquid xenon detectors which were constructed to optimize light collection efficiency. At the same time, a comprehensive model of scintillation and ionization processes in xenon known as the NEST [20–22], developed with simple phenomenological models and based on consideration of world data, is gradually being adopted in the xenon field. The values of the relative scintillation efficiency ($L_{eff}$) from NEST decrease continuously down to zero energy, which is consistent and slightly lower than that from an independent phenomenological calculation [23]. These developments call for careful reexamination of the low-mass WIMP sensitivity using xenon detectors. In Ref. [13], we reported the first 17.4 live days null search results in PandaX-I. In this paper, we present an improved analysis including the full PandaX-I data set, starting from May 26, 2014 to October 16, 2014, with a total of 80.1 live-day exposure in the search for dark matter. We shall refer to these data as dark matter search data in the remainder of this paper.

## II. THE PANDAX-I EXPERIMENT

PandaX is a dual-phase liquid xenon dark matter experiment [24] located at the China Jin-Ping Underground Laboratory (CJPL) [25]. The first phase PandaX-I is a pancake-shaped 120 kg detector optimized for light collection targeted for low-mass WIMPs [13,24]. The xenon chamber is a stainless steel inner vessel with an inner diameter of 750 mm, housing approximately 450 kg of liquid xenon. The entire inner vessel sits in an outer vacuum vessel constructed from 5-cm thick high-purity oxygen-free copper serving also as a radon barrier and electromagnetic shield, and enclosed by a passive shield made of copper, polyethylene, lead, and polyethylene, from inner to outer layers. The gap between the outer vessel and the passive shield is continuously flushed with boil-off nitrogen to maintain a radon level of less than 5 Bq/$m^3$, more than a factor of 20 below the level in the experimental hall. The central time-projection chamber (TPC) is a cylinder with a diameter of 60 cm and a height of 15 cm confined by a cathode grid (−15 kV) at the bottom, a gate grid (−5 kV) and an anode mesh (ground) separated by 8 mm, below and above the liquid level respectively, and a surrounding polytetrafluoroethylene (PTFE) reflective wall. After a particle-xenon interaction, prompt scintillation photons (S1 signal) are produced in the liquid. Ionized electrons are then drifted vertically upward by an induced drift field and extracted into the gas by an extraction field, producing the electroluminescence (S2 signal). A top photomultiplier tube (PMT) array consists of 143 Hamamatsu R8520-406 (1-in square) tubes and a bottom array holds 37 Hamamatsu R11410-MOD (3-in circular) tubes. The PMTs view the active volume, collecting photons from both the S1 and S2 signals, with the bottom array dominating the light collection for both S1 and S2 signals. The radioactivity from the bottom PMT array is shielded by a layer of 5-cm thick LXe between the cathode and the PMT surface. The average dark rate per tube, i.e. the rate of random single photoelectrons (PEs), is 0.06 and 1.07 kHz for top and bottom PMTs, respectively. The time separation between S1 to S2 signals gives the vertical position of the interaction, and the horizontal position is encoded in the S2 charge pattern in the PMT arrays. Multiple scatter events can be identified from the data by events which contain multiple S2 signals, either separated in time if they happen at different vertical positions or separated in the horizontal plane if there are multiple charge clusters in the PMT pattern. Gamma-ray background produces electron recoil (ER) events whereas the dark matter signal produces nuclear recoil events. The ratio of S1 and S2 signal area gives a powerful means of ER rejection when looking for DM-like NR signals [26].

The PMT waveforms, amplified by a factor of 10 using Phillips 779 amplifiers, are recorded by CAEN V1724 14-bit 100 MS/s digitizers. The trigger for the data acquisition system (DAQ) is generated based on the majority outputs from the five digitizer boards for the bottom PMT arrays. For low-energy signals in the dark matter region, the trigger is generated by S2 with a threshold of about 89 total PE, whereas higher-energy events were triggered primarily by S1 with a charge threshold of about 65 PE. Each readout window is 200 $\mu$s long, with approximately equal division of pre- and post-trigger readout times. The PMTs are balanced to a gain of $2 \times 10^6$, with a recorded amplitude

TABLE I. Summary of data taken during the entire PandaX-I running period.

| Run type | DAQ Time (hr) | Live Time (hr) | Trigger Rate (Hz) |
|---|---|---|---|
| DM | 2,158.32 | 1,923.11 | 3.58 |
| $^{252}$Cf | 95.32 | 94.05 | 17.95 |
| $^{60}$Co | 405.14 | 361.47 | 22.23 |

of the single photoelectrons roughly at 60 digitizer bits. To save data volume, segments with waveform samples less than 20 digitizer bits from a preloaded baseline are zero-suppressed. For nonsuppressed segments, 40 time samples before and after the 20 bit threshold crossing are recorded.

Three types of data runs were taken during the PandaX-I running period, the WIMP search, $^{60}$Co ER calibration, and $^{252}$Cf NR calibration runs. A summary of the data taken is given in Table I. Various cuts (discussed below) are applied to remove periods with unstable operating conditions, leading to a difference between DAQ time and the live time.

Two independent analyses were developed within the collaboration, utilizing different signal window selection, signal identification and reconstruction, event selection cuts and efficiencies, as well as the final fitting method. The two analyses were thoroughly cross-checked at various analysis stages, yielding consistent results. In the remainder of this paper, we will elaborate on one of the analyses, and the other one is detailed in Ref. [27].

## III. DATA PROCESSING AND SELECTION CUTS

A number of improvements have been made in the data analysis pipeline compared with the first results [13]. We shall describe the general procedure in steps below, with major improvements highlighted.

The raw data files are screened for basic data quality before being processed for physics analysis. Detection of PMT high-voltage outages is applied to filter data sets with low light collection. A nominal trigger rate below 10 Hz is required to reject those data sets which are seriously contaminated by noise during times when running conditions are poor. Files with unexpected discharges from electrodes can be discriminated using the average number of S1-like and S2-like signals in a waveform. If containing an average of larger than 40 S1-like or 10 S2-like signals, the events will be removed. Dark rates from PMTs are tracked and used to characterize the stability of the detector. A low random coincidence rate is essential and a cut is developed on PMT dark rates to minimize contamination.

Baseline subtraction is performed on each waveform. In this analysis, the baseline is calculated based on the pre-samples from each waveform segment to suppress the drift and overshoot of baselines, whereas in Ref. [13] only weekly calibrated baselines were loaded. This update caused a downward shift of the light yield of approximately 6% at 40 keV$_{ee}$ electron-equivalent energy.

Several malfunctioning PMTs are inhibited in the analysis. During operation, four bottom PMT channels gradually developed connection problems, manifest as improper base resistance or capacitance, and were inhibited in the analysis to avoid a time-dependent light yield. Among the rest of the bottom PMTs, a number of them experienced excessive dark rate (10 kHz and above) during the run but could sometimes be recovered through power cycling or lowering the corresponding high voltage. One channel was fully inhibited due to unstable dark rate. The channel inhibition led to another 10% reduction in light yield. On average, two to three bottom PMTs had to run at a lower gain ($<1 \times 10^6$) to maintain a manageable dark rate. For the top array, seven PMTs gradually developed problems during the run and were inhibited as the problem showed up, but this has little impact on the analysis presented here.

Gain correction was applied to baseline-subtracted waveforms based on the results of weekly LED calibration runs. A hit finder algorithm identifies signal hits channel by channel while tagging noise primarily due to the periodic 200 kHz electromagnetic interference from the CAEN PMT high-voltage supplies, occasionally fluctuated above the 20 bit zero-suppression threshold. The waveform is then integrated in the "hit window" to define the hit charge. The hits in different channels are then clustered in time using an improved charge-dependent algorithm with high efficiency for in-time short S1 signals while avoiding splitting a low charge but wide S2 into multiple clusters. For each cluster, a software sum is formed on all digitized channels, from which one computes the full-width-half-maximum, the full-width-1/10-maximum, as well as the number of peaks in the cluster. A binary decision tree method is developed to sort any given cluster into S1-like and S2-like signals based on these variables. The identification efficiency is verified to be nearly 100% by visually checking waveforms of thousands of identified clusters.

We developed further signal-level cuts to identify spurious noise in the S1-like and S2-like signals. For S1-like signals, we employed a further ripple-pattern cut on the software-summed waveform, a cut on the ratio of charge computed from the summed waveform to the total hit charge,[1] and a cut on the ratio of the total number of noise hits to the total hits in the cluster. In addition, cuts are placed on the ratio of the height to area and that of the height to width. To avoid signals from afterpulsing, S1 signals are required to be before the first good S2 signal. For S2, we developed a shape symmetry cut to remove events very close to the anode when S1 and S2 cannot be

[1]The summed waveforms for the 200 kHz noise tend to show a clear ripple feature, leading to a cancellation in the corresponding charge.

easily separated in time, identifying those events with a characteristic sharp spike at the beginning of the S2 pulse. In addition, an S2-like signal will be discarded if its ratio to the largest S2 is less than 1% or if such a signal is consistent with a single-electron S2 with charge less than 30 PE; the inefficiency due to these two cuts is estimated to be negligible by a Monte Carlo (MC) simulation.

Periods with unstable overall PMT signal rates were identified during the run, possibly due to small discharges on the electrodes, producing light pulses. In addition to the earlier file-by-file cuts, a number of tighter data quality cuts were placed event by event to search for "dirty waveforms," including a cut on the total number of S1-like signals, the ratio of S1 to total charge before the first S2, and the ratio of the sum of S1 and S2 to the total charge (which also suppresses multiple scattering events). To avoid ambiguity due to multiple S1-like signals per event, we require that the number of S1 should be either one or two, and in case of the latter the maximum S1 is identified as the primary if the charge of the second S1 does not exceed 50% of the first. Finally, to suppress accidental background, we placed a three-hit coincidence cut on any good signal, and a 300 PE cut on S2 (discussed later).

Finally, S1 and S2 signals are reconstructed into physical events. The vertical position is determined by the separation between S1 and S2 signals, assuming a drift speed of 1.7 mm/$\mu$s under the drift field of 0.67 kV/cm [13,28]. The horizontal position of the interaction is reconstructed with the S2 PMT charge pattern using multiple algorithms. As an improvement to the charge center of gravity (CoG) method, we developed a fast charge pattern template matching (TM) method. The expected charge templates were generated using a custom GEANT4 [29] based Monte Carlo which simulates optical photon propagation from S2 signals in the PandaX-I TPC geometry, identical to the templates used in the fast artificial neural network (FANN) reconstruction method developed by the independent analysis. The difference in the horizontal positions from the FANN and TM methods is on average 5 mm, obtained using 40 keV deexcitation events from neutron calibration data. This is independent of the radial and vertical positions and consistent with the expected position resolution from MC. In the analysis presented here, the TM reconstruction is chosen. To identify multiple scattering at the same vertical location, we set a charge clustering cut by requiring that the horizontal distance between the CoG and TM positions be less than 55 mm.

## IV. DETECTOR CALIBRATIONS

The PandaX-I detector has been carefully calibrated using various methods to perform an effective search for low-mass WIMPs. Single-electron events were identified to calibrate the single-electron gain (SEG) in the electroluminescence. Neutron-activated x rays were used to determine the photon detection efficiency for S1 (PDE) of the PMTs which signifies the sensitivity of our detector in the low-mass region, and the electron extraction efficiency (EEE) from the liquid. A neutron calibration with $^{252}$Cf was used to generate the NR events that were used to define the DM search window. Finally, a gamma calibration with $^{60}$Co was used to find the leakage of ER background into the search window.

Neutron calibrations have been taken several times throughout the run with a total exposure of 95 hours (see Table I). The 40 keV ($^{129}$Xe) and 80 keV ($^{131}$Xe) inelastic recoil x rays are used in calibrating the uniformity for both S1 and S2 in the detector. For a fixed energy deposition in the detector, the PMT arrays see different light and charge yields depending on the spatial location of the event, which must be corrected to a detector average before further analysis is performed. The uniformities for S1 and S2 are verified to be decoupled in the vertical direction and horizontal plane. The horizontal variation of 40 keV S2 peaks in the 54.0 kg fiducial volume is measured to be $\pm 36\%$, which dominates the detector nonuniformity. The vertical uniformity for the S2 signals, characterized by an exponential "electron lifetime," reflects the electronegative impurity level in the detector which tends to attenuate the charge signal during drifting. The average electron lifetime in our detector is fit with a decaying exponential and determined to be $328 \pm 8$ $\mu$s (an attenuation length of about 60 cm as compared to the 15 cm maximum drift distance). On the other hand, the variation of the S1 peak in the fiducial volume in the vertical (horizontal) direction is $\pm 8.5\%$ ($\pm 9.5\%$). All discussions in the remainder of the paper are made with the uniformity corrections taken into account.

One of the important properties of the detector is SEG, the average number of PEs observed in PMTs from single-electron electroluminescence. It can be determined from the PE distribution of the smallest S2 signals taken at any normal detector run, fit with a double Gaussian function with means related by a factor of 2 from the charge quantization (see Fig. 1). The SEG is determined to be $18.4 \pm 1.6$ PE/e, where the uncertainty is estimated by varying parameters in the hit clustering algorithm as well as the fitting function and range.

The PDE and EEE can be determined from the 40 and 80 keV x-ray events during the neutron calibration. The events collected are shown in the S2 vs S1 plot in Fig. 2. The location of the 40 keV peak (with decay time less than 1 ns) is at 178.8 PE in S1, with an average 11.6 PE mixture from the associated NR, estimated from the pure NR events seen at low energy as well as through MC. At this energy, our detector has a S1 photon yield of 4.2 PE/keV. Using the NEST-0.98 model [21], this corresponds to 6.0 PE/keV at zero electric field at the standard 122 keV, in comparison to the 3.9 PE/keV obtained in XENON100 [11] and 8.8 PE/keV in LUX [12].

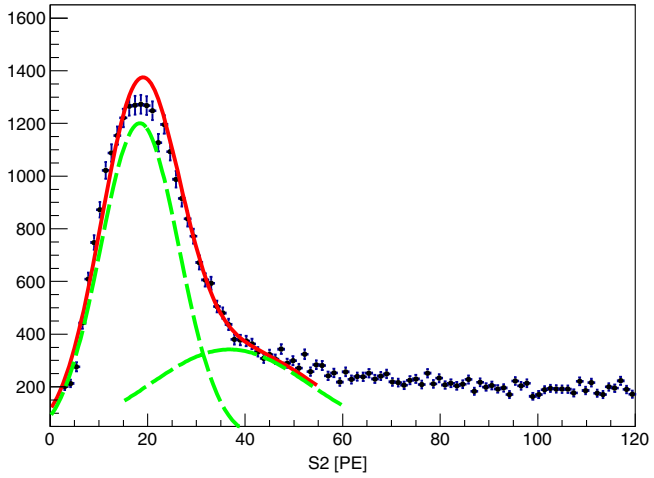


FIG. 1 (color online). The PE distribution of the smallest S2 signals (corrected for horizontal nonuniformity), summed over all top and bottom PMTs. The single-electron gain is determined by fitting two constrained Gaussians, shown as the dashed green lines.

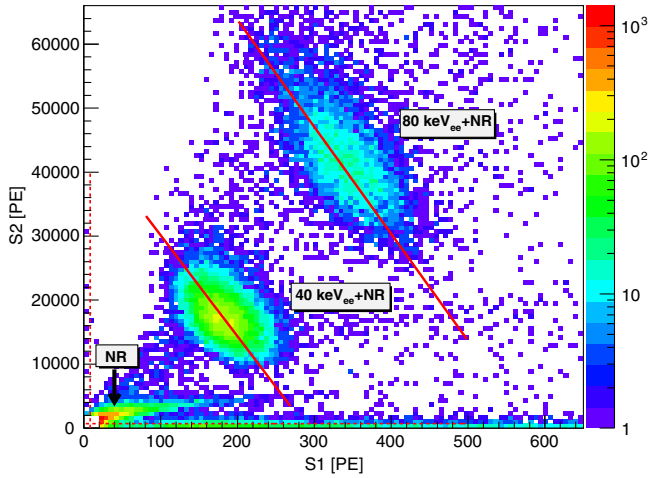


FIG. 2 (color online). Distribution in uniformity-corrected S1 and S2 for the deexcitation gamma peaks in the neutron calibration runs. The antidiagonal lines are the anticorrelation fit at the two energies. The dashed vertical and horizontal lines indicate the mean NR energy in mixture with the gamma energies at 40 and 80 keV.

The electron-equivalent energy of a given event can be reconstructed from the light and charge outputs as

$$E_{\rm rec} = ({\rm S1}/{\rm PDE} + {\rm S2}/{\rm SEG}/{\rm EEE}) \times W, \qquad (1)$$

where $E_{\rm rec}$ is the reconstructed energy in keV$_{ee}$ splitting into scintillation and ionization parts, and $W = 13.7$ eV is the average energy to produce a scintillation photon or to liberate an electron [20]. The anticorrelated fluctuations in the light and charge outputs due to electron-ion recombination is naturally accounted for in Eq. (1). Similar to Ref. [13], we performed anticorrelation fits using Eq. (1) to

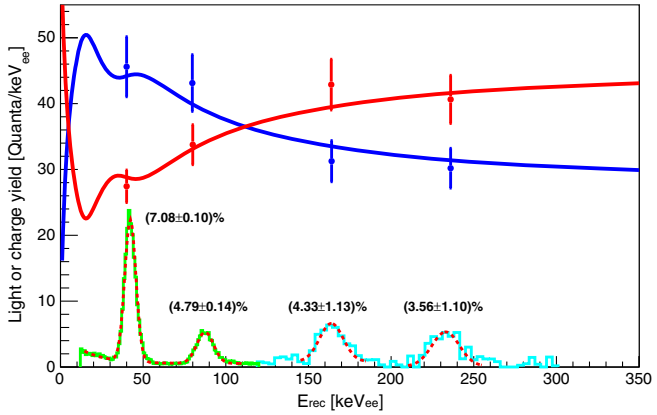


FIG. 3 (color online). The $L_y$ (blue) and $C_y$ (red) (in units of quanta per keV$_{ee}$) extracted based on PDE and EEE obtained at different energies overlaid with corresponding curves predicted by NEST-0.98. The reconstructed energy spectra for the deexcitation peaks and metastable xenon isotopes are also overlaid with the $y$ axis scaled for visual clarity with fitted energy resolutions indicated in the figure.

the 40 and 80 keV deexcitation peaks, as well as the neutron-induced metastable $^{129m}$Xe (164 keV) decay gamma rays after the neutron calibrations.[2] The PDE (EEE) determined with the 40 keV$_{ee}$ peak is 9.6% (82.1%). The fractional uncertainties are estimated to be 10% and 9%, respectively, based on the difference in values obtained at the other two energies, as well as those in Ref. [13].

To facilitate the comparison of our data with the model prediction, we convert the peaks in S1 and S2 into a per unit energy total photon yield ($L_y$) and charge yield ($C_y$), using

$$L_y = \langle S1\rangle/{\rm PDE}/E_{\rm rec},$$
$$C_y = \langle S2\rangle/{\rm SEG}/{\rm EEE}/E_{\rm rec}, \qquad (2)$$

where $\langle S1\rangle$ and $\langle S2\rangle$ here refer to the location of corresponding peaks in the distribution. In Fig. 3, our measured data is compared to the mean values in NEST-0.98 [21] under the same drift field. Reasonable agreement is found at all four energy peaks in $^{252}$Cf data (40, 80, 164, 236 keV). The uncertainties shown in the figure, aside from the statistical uncertainties in the peak determinations, arise from the systematic uncertainties of the PDE and EEE determination through the anticorrelation fits.

In the $^{252}$Cf NR calibration runs, the single events at very low energy with S1 $< 30$ PE are expected to have less than 1% contamination from the ER band based on MC simulations, and the latter can therefore be neglected. The distribution of these low-energy events in $\log_{10}$(S2/S1) vs S1 is shown in Fig. 4(a). It can be seen that there are

[2]We did not perform anticorrelation fits for the $^{131m}$Xe 236 keV gamma lines since it was difficult to separate the peak cleanly from the background.

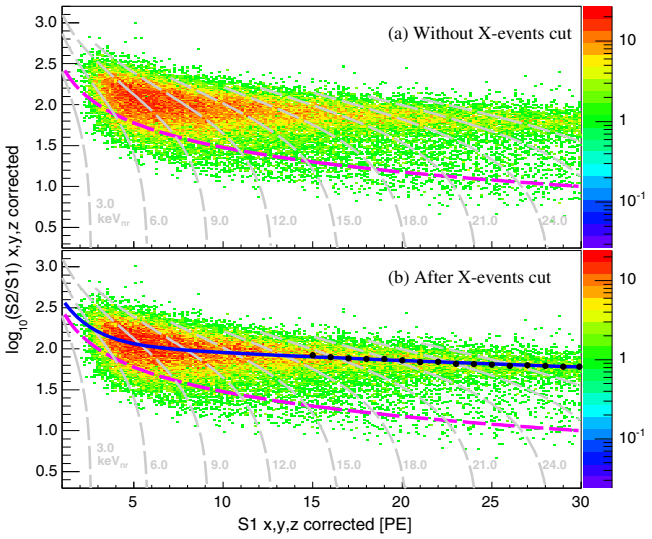


FIG. 4 (color online). The band of $\log_{10}(S2/S1)$ vs S1 for the NR calibration data without (a) and with (b) the "X" cut. See text for definition of the cut. The 54.0-kg fiducial cut is applied. The solid blue line in panel (b) is the median of the pure NR band in MC, and the dots are the Gaussian mean obtained from the data for S1 > 15 (where the detection efficiency is flat so that the data and MC comparison is straightforward). The dashed magenta lines in both panels are the 300 PE cut on S2, below which no dark matter candidate is considered. The gray dashed lines are the equal-energy lines with NR energy indicated in the panels.

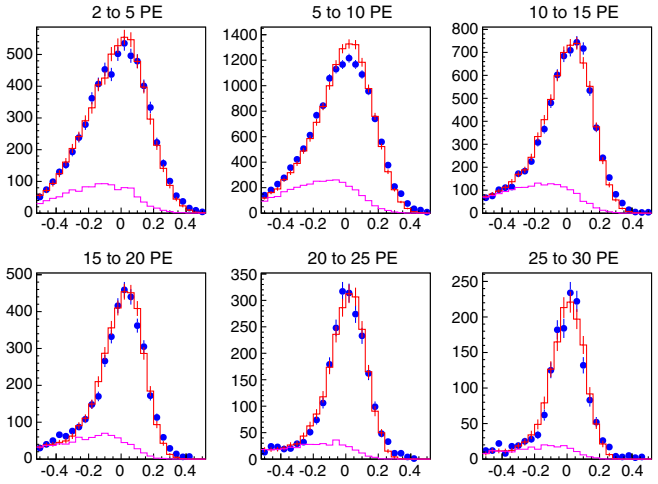


FIG. 5 (color online). Comparison of the distribution of $\log_{10}(S2/S1)$ in the NR data and tuned MC in six slices of S1 as indicated by the panel titles: data (blue), tuned "neutron-X" events in the MC (magenta), and the sum of pure NR and tuned "neutron-X" in MC (red). In each slice of S1, the value of $\log_{10}(S2/S1)$ is shifted relative to the median value in that slice. The efficiency in Fig. 6 has been applied to the MC to compare with the data.

scattered events with suppressed S2, producing an asymmetric NR band. Based on the charge pattern of S1 signals, it was determined that such events (called "X" events [30]) are due to multiple scattering of neutrons with some energy deposition in the "chargeless" region, either below the cathode, or in the xenon "skin" between the PTFE wall and the stainless steel inner vessel (viewed partially by the outermost ring of the top PMT array). They have to be properly taken into account to correctly calibrate the NR efficiency.

To compare the data with expectation, a GEANT4 MC is developed to simulate the $^{252}$Cf runs, which produces both single-scatter pure NR and "neutron-X" recoil spectra, and employs the NEST-0.98 nuclear recoil model [21] with the PDE, EEE and the SEG obtained above. After global tuning of the strength of the "neutron-X" events in the MC, excellent agreement is found in different slices of S1 between the data and MC (Fig. 5).[3] If the new NEST-1.0 model [22] is used instead, the MC can also be tuned to agree with the data by increasing the EEE by 2%, much less than its assigned uncertainty. The tuned MC is used as the true physical distribution to extract the NR efficiency.

To suppress the "X" events, a charge asymmetry cut between the top and bottom PMT arrays as well as a cut on the ratio of the maximum single PMT charge to the total on S1 were applied to all data including $^{252}$Cf, $^{60}$Co, and DM data sets. The NR distribution after the cut is shown in Fig. 4(b), where the low S2 "X" events are significantly reduced. Our overall analysis cut efficiency for NR events with S1 > 10 PE is estimated by comparing the number of $^{252}$Cf events in (S1,S2) bins before and after all cuts in this energy region, and an approximately uniform 77.5% value is obtained. At lower energy, the overall NR efficiency is estimated by taking the ratio of the measured distribution to the tuned MC, anchored at 77.5% at higher energy. The

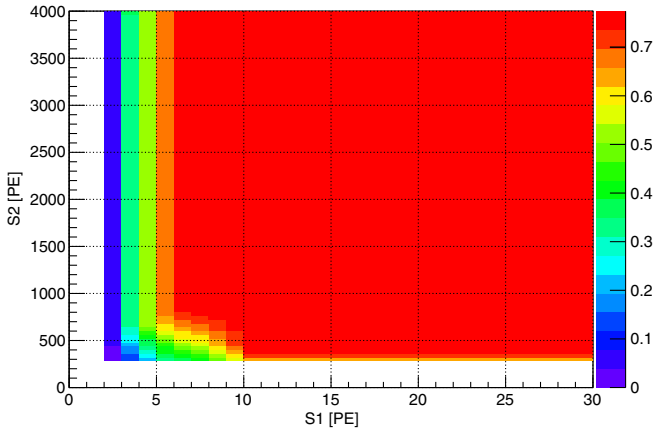


FIG. 6 (color online). The nuclear recoil efficiency in (S1,S2) determined using the method discussed in the text.

[3]A fluctuation of 17% from the gas gain, in addition to the nominal statistical fluctuations introduced by NEST, helps to match the measured width in each S1 slice.

resulting two-dimensional distribution of the NR efficiency is shown in Fig. 6.

The ER calibration is performed with a $^{60}$Co gamma source, interleaved frequently during dark matter search data taking. Low-energy $\gamma$ rays are produced through the well-known Compton scattering mechanism. The distribution of the single scatter ER events in $\log_{10}(S2/S1)$ vs S1 is shown in Fig. 7(a). All cuts, including a fiducial cut, have been applied. For events with S1 between 2 and 30 PE, 12 out of 1520 events were located below the median of NR in $\log_{10}(S2/S1)$. Subtracting the expected 1.65 events from accidental coincidence (see later discussions), the remaining ER leakage is $0.68 \pm 0.23\%$ of the total, consistent with a pure Gaussian expectation (0.5%) obtained by fitting the ER band distribution.

Within the S1 range of 10 to 30 PE, the efficiency for ER detection and selection is estimated to be 75.7% by taking the ratio between the final number of events after all cuts and the raw events on the ER band. At lower energy, the efficiency is estimated by taking the ratio between the measured and expected S1 spectrum from MC with 75.7% at higher energy as an anchor [shown in Fig. 7(b)]. The overall efficiency is approximately 71.5% in the entire 2–30 PE range.

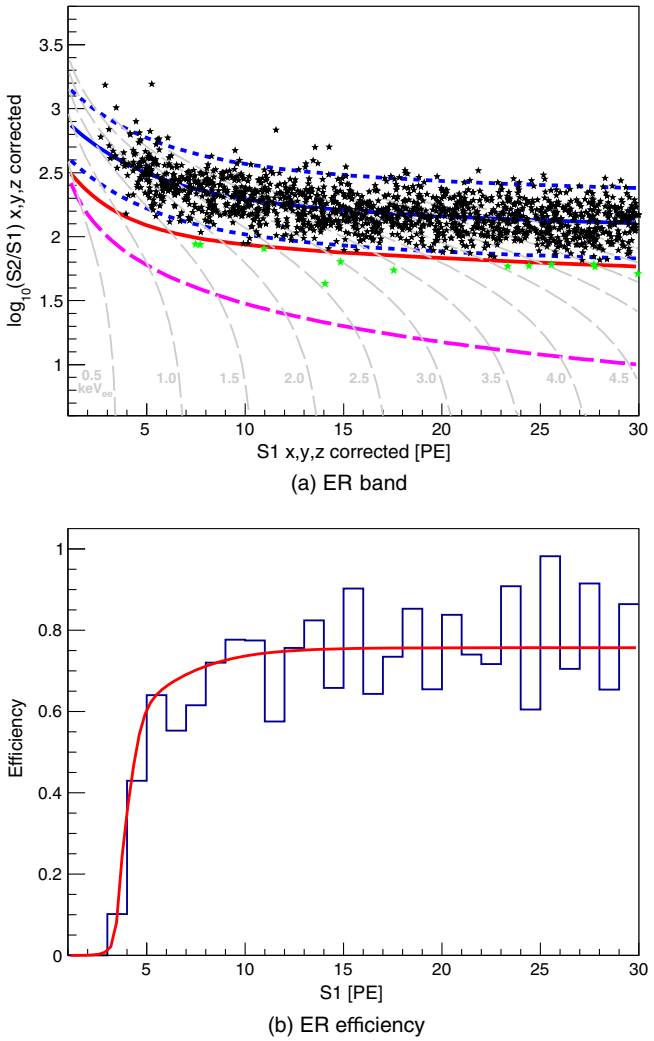


FIG. 7 (color online). (a) The band of $\log_{10}(S2/S1)$ vs S1 for the $^{60}$Co ER calibration runs with the median and $\pm 2\sigma$ of the band indicated as the solid and dashed blue lines, respectively. The median of the NR band is indicated as the solid red line, below which the 12 leaked events are plotted as green markers. The dashed magenta line is the 300 PE cut on S2. The gray dashed lines are the equal-energy lines with ER energy indicated in the figures. (b) The ER efficiency in S1 obtained by taking the ratio between the data and MC (histogram), and the red curve is a fit to the efficiency.

## V. BACKGROUNDS IN DARK MATTER SEARCH DATA

The low-energy dark matter window was blinded in the analysis until all data cuts were determined. The cuts on S1 and on the fiducial volume were optimized from a figure-of-merit based on the expected below-NR-median backgrounds of the ER, the accidental background (statistically determined from data), and the neutron background (MC estimates). The final optimized search window on S1 is from 2 to 30 PE, and that on S2 is 300 to 10 000 PE. The fiducial cut is determined as $r^2 < 500$ cm$^2$ with a drift time between 10 to 80 $\mu$s, resulting in a fiducial mass of $54.0 \pm 2.3$ kg. In what follows, we shall discuss the background contributions in the dark matter search.

*a. ER background:* Expected ER background in our final candidate sample with all cuts imposed, summarized in Table II, has been estimated with a GEANT4-based MC program, with a few updates compared to that in Ref. [13]. First, by taking into account the additional energy deposition in the below-cathode region ("X" events) observable through PMT arrays, some of the MC events shifted above the dark matter search window, leading to a reduction of background from almost all components. Second, the

TABLE II. The expected and observed background rates in the fiducial volume and in the dark matter search window. mDRU $= 10^{-3}$ evt/day/kg/keV$_{ee}$. Uncertainties in the MC prediction originate from uncertainties in the material radioactivity screening, except those for Rn and Kr which are due to the uncertainties in the PandaX data.

| Source | background level (mDRU) |
|---|---|
| Top PMT array | $4.7 \pm 2.3$ |
| Bottom PMT array | $2.3 \pm 1.5$ |
| Inner vessel components | $3.8 \pm 2.2$ |
| TPC components | $1.9 \pm 0.9$ |
| $^{85}$Kr | $2.6 \pm 1.2$ |
| $^{222}$Rn and $^{220}$Rn | $0.5 \pm 0.2$ |
| Outer vessel | $0.9 \pm 0.6$ |
| Total expected | $16.7 \pm 3.9$ |
| Total observed | $23.6 \pm 3.5$ |

radioactivity level of the stainless steel vessel was updated with a counting measurement with much better statistics, also resulting in a reduction in background expectation. Third, the internal $^{85}$Kr, $^{222}$Rn and $^{220}$Rn levels were studied with the statistics of the full dark matter search data sample with the same delayed coincidence techniques as in Ref. [13]. The measured Kr concentration in Xe is $68 \pm 29$ ppt mole/mole (the uncertainties are mainly due to event selection methods in the analysis) assuming a $2 \times 10^{-11}$ isotopic abundance of $^{85}$Kr, leading to an expected background of $2.6 \pm 1.2$ mDRU based on the MC. The $^{222}$Rn and $^{220}$Rn backgrounds were determined to be $0.7 \pm 0.2$ and $0.15 \pm 0.06$ mBq in the fiducial volume, respectively, with uncertainties primarily arising from event selection cuts. The resulting background of $0.5 \pm 0.2$ mDRU in the dark matter energy and fiducial volume search window is estimated by MC with an improved treatment taking into account the nonsecular equilibrium due to the long-lived isotope $^{210}$Pb ($\tau =$ 22.2 year). The overall ER background in the dark matter search data estimated from radioactivity counting is $16.7 \pm 3.9$ mDRU. This is consistent with the ER background 23.6 mDRU extrapolated from events with S1 $> 30$ after efficiency correction ($\pm 15\%$ depending on the energy cut as well as efficiency modeling), assuming a flat distribution of the ER background in keV$_{ee}$ at very low ER energy based on the MC.

The real relevant ER background for dark matter searches is formed from events that leak below the NR median, including those due to detector effects as well as the so-called "gamma-X" events with partial energy deposition in the "chargeless" regions. To reliably estimate the number of such events, it is best to use the ER calibration data where such events are included with the right proportion.

*b. Neutron background:* The neutron background is estimated using a combination of SOURCES-4A[31] and GEANT4 simulation, leading to an estimate of 1.45 events within the $54.0 \times 80.1$ kg-day exposure before efficiency cuts, and about 0.35 events after all cuts. This yields 0.18 neutron background events below the NR medium line. We assign a generous 50% uncertainty to the MC estimate. Alternatively, a 90% confidence level upper limit of 1.15 neutron events can be set based on the single to multiple NR scattering ratio from the MC and the absence of the multiple scattering NRs in the dark matter search.

*c. Accidental background:* In our dark matter search data, we find a significant number of isolated S1 and S2 events, which yield a substantial background. An isolated S1 is an event occurring without an obvious S2 nearby. These signals are likely from multiple origins, e.g. light leaking into the TPC due to interaction in the skin region, small discharges in the TPC due to impurities or high voltage, and the accidental coincidence of SPE between PMTs. An isolated S2 is an event without an S1 proceeding the waveform, which can be due to events with very low energy of which S1 cannot be detected. In addition, based on a visual inspection of isolated S2 events, it was noticed that a significant fraction of such events have a spiky timing profile at the beginning of S2 (but cannot be efficiently rejected with existing algorithms), implying that these S2 events happened very close to the gate grid where S1 and S2 can no longer be separated.

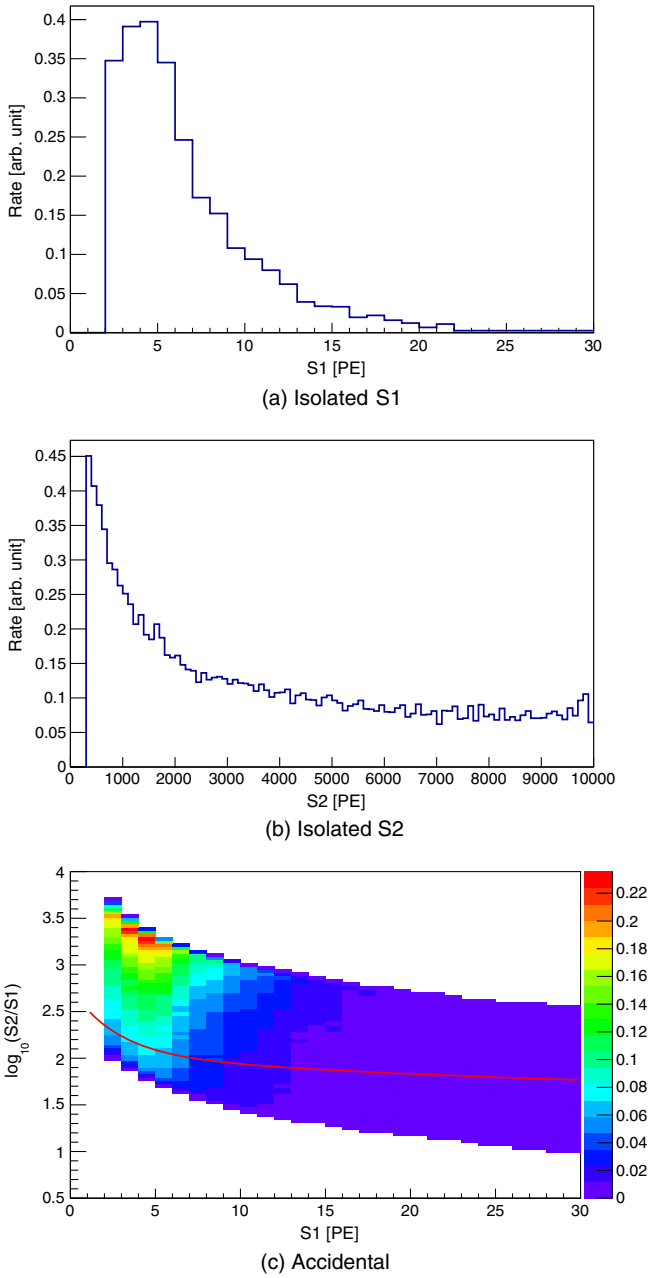


FIG. 8 (color online). The measured isolated S1 (a) and S2 (b) charge spectra, and the band of $\log_{10}(S2/S1)$ vs S1 (c) for the statistically obtained accidental background, with the sharp cutoffs at the top and bottom corresponding to the 10 000 and 300 PE cut. The median of the NR band is indicated as the red line.

In our dark matter search data, isolated S1 events are estimated by looking for uncorrelated S1 events before a

large S1 (which is associated with a trigger) yielding a rate of about 23 Hz, with the charge distribution shown in Fig. 8(a). Isolated S2 events are measured with a rate of about 240 events/day for S2 within 300 to 10 000 PE (the 300 PE cut is imposed to balance between the suppression of such background and the loss of low-energy sensitivity), without obvious nonuniformity in the horizontal plane. The charge spectrum of such S2 signals is shown in Fig. 8(b). The rate of such events in the $^{60}$Co calibration runs increased to about 568 events/day, and the amount of the rate increase is consistent with the MC expectation.

Isolated S1 and S2 events produce accidental coincidences which mimic real events. Such background can be statistically evaluated by forming random pairs in S1 and S2, and the resulting distribution in $\log_{10}(S2/S1)$ vs S1 is shown in Fig. 8(c). The overall rate in the dark matter search data is estimated to be 35.1 events in 80.1 days with a conservative 10% uncertainty based on the statistical uncertainty of a day-long dark matter search run.

## VI. CANDIDATE EVENTS FROM 80.1 DAY DARK MATTER SEARCH DATA

For the dark matter search data, the event rates after different levels of cuts are summarized in Table III. The data quality cuts remove a large fraction of the multiple scattering events, reducing the total number considerably, which also explains that the subsequent single-site cut has a small effect on the remaining number of events. Within prescribed cuts, 542 events were found in 54.0 kg × 80.1 days. The event distribution in $r^2$ vs drift time in the TPC is shown in Fig. 9(a). The event projections in $r^2$ (with two position reconstruction methods) and drift time are also compared to the expected ER distribution from the Monte Carlo, where good agreement is achieved.

The distribution of events in $\log_{10}(S2/S1)$ vs S1 is shown in Fig. 10. The majority of the events are consistent with an ER origin. The events located higher than the ER band at low S1 are the accidental backgrounds, more prominent than those in the $^{60}$Co calibration run due to the much lower ER event rate in the dark matter search data. Seven of the candidate events are located below the median of the NR band indicated by the green markers in Figs. 9(a) and 10. For comparison, the expected background in the

TABLE III. The event rate in the DM run after various levels of analysis cuts.

| Cut | # Events | Rate (Hz) |
|---|---|---|
| All triggers | 24,762,972 | 3.58 |
| Quality cut | 6,127,280 | 0.88 |
| Single-site cut | 5,050,845 | 0.73 |
| S1 range (2–30 PE) | 62,872 | $9.08 \times 10^{-3}$ |
| S2 range (300–10 000 PE) | 44,171 | $6.38 \times 10^{-3}$ |
| Fiducial volume | 542 | $7.83 \times 10^{-5}$ |

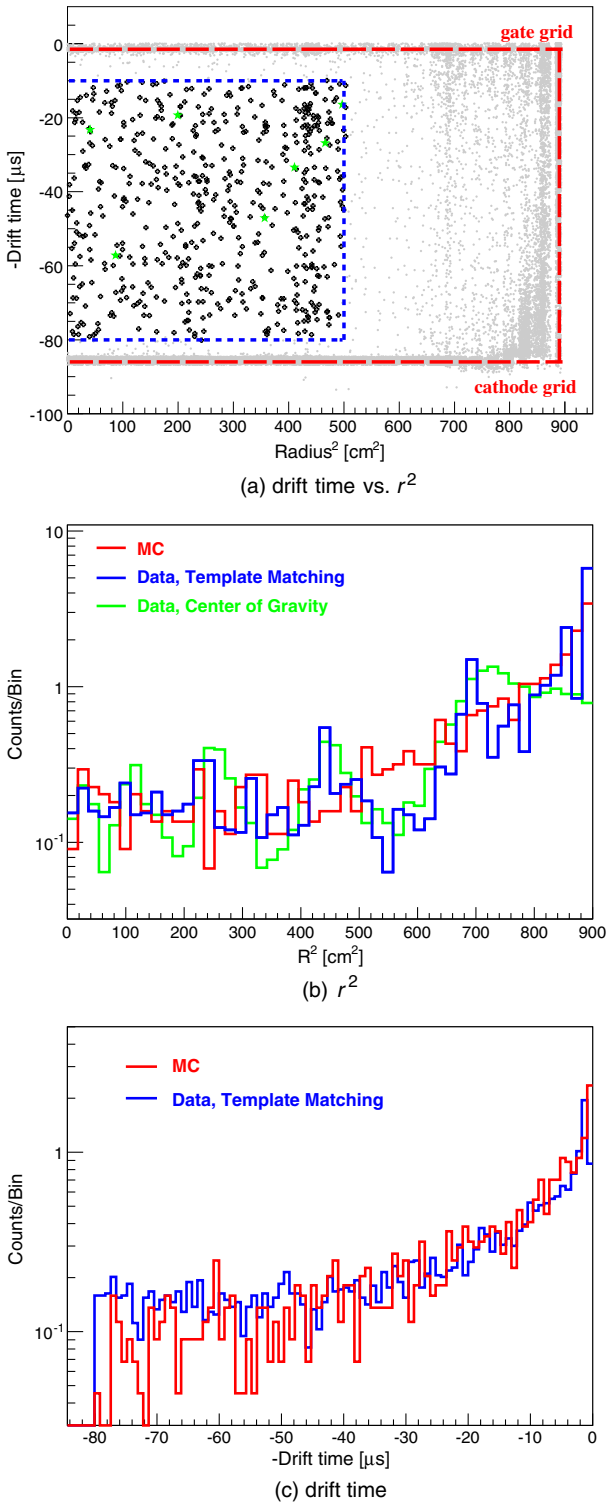


FIG. 9 (color online). (a) The vertex distribution of events in the TPC during dark matter search data taking. The blue dashed box indicates the fiducial volume, and the red dashed box indicates the entire active volume within the TPC, confined by the cathode, gate grid, and the PTFE wall. The events below the NR median are indicated by the green markers. (b) Projection in $r^2$, with data (TM method for position reconstruction) in blue, data (CoG method) in green, and the MC energy deposition CoG in red, (c) Projection in the drift time, with data (TM) in blue and the MC energy deposition CoG in red.

total sample as well as those below the NR mean is shown in Table IV. The ER background is estimated based on the 23.6 mDRU value, a corresponding ER energy range of 6.9 $\mathrm{keV_{ee}}$, and an average ER efficiency of 71.5%. The below-NR-median accidental background is estimated based on the distribution in Fig. 8(c). Summing over all the contributions, we expect 6.9 background events below the NR median. No significant excess above the background is observed.

## VII. FITTING METHOD

To maximally use the information from the data, instead of choosing only the below-NR-median region to search for DM like in Ref. [13], in this analysis we defined a much extended DM window with S1 between 2 and 30 PE and S2 between 300 to 10 000 PE. To fit all data, an unbinned extended likelihood function is constructed as

$$\mathcal{L} = \mathrm{Poisson}(N_{\mathrm{m}}|N_{\mathrm{exp}}) \times \Pi_{i=1}^{i=N_m}\left[\frac{N_{\mathrm{DM}}(1+\delta_{\mathrm{DM}})P_{\mathrm{DM}}(\mathrm{S1}^i,\mathrm{S2}^i)\epsilon_{\mathrm{NR}}(\mathrm{S1}^i,\mathrm{S2}^i)}{N_{\mathrm{exp}}} + \frac{N_{\mathrm{ER}}(1+\delta_{\mathrm{ER}})P_{\mathrm{ER}}(\mathrm{S1}^i,\mathrm{S2}^i)}{N_{\mathrm{exp}}} + \frac{N_{\mathrm{Acc}}(1+\delta_{\mathrm{Acc}})P_{\mathrm{Acc}}(\mathrm{S1}^i,\mathrm{S2}^i)}{N_{\mathrm{exp}}} + \frac{N_{nbkg}(1+\delta_{nbkg})P_{nbkg}(\mathrm{S1}^i,\mathrm{S2}^i)\epsilon_{\mathrm{NR}}(\mathrm{S1}^i,\mathrm{S2}^i)}{N_{\mathrm{exp}}}\right] \times G(\delta_{\mathrm{DM}},0.2)G(\delta_{\mathrm{ER}},0.15)G(\delta_{\mathrm{Acc}},0.1)G(\delta_{nbkg},0.5), \quad (3)$$

where $N_m$ and $N_{\mathrm{exp}}$ are the total number of measured and fitted candidates with

$$N_{\mathrm{exp}} = N_{\mathrm{DM}}\langle\epsilon_{\mathrm{NR}}\rangle_{\mathrm{DM}}(1+\delta_{\mathrm{DM}}) + N_{\mathrm{ER}}(1+\delta_{\mathrm{ER}}) + N_{\mathrm{Acc}}(1+\delta_{\mathrm{Acc}}) + N_{nbkg}\langle\epsilon_{\mathrm{NR}}\rangle_{nbkg}(1+\delta_{nbkg}). \quad (4)$$

As indicated in Fig. 9, the position dependence of events in the fiducial volume is rather weak and is therefore ignored here for simplicity. $N_{\mathrm{DM}}$ ($N_{nbkg}$) is the total number of WIMP particles (neutrons) interacting with the detector during the measurement before efficiency and acceptance cuts. $N_{\mathrm{DM}}$ is computed for each given pair of WIMP mass and cross section $(m_\chi, \sigma_{n-\chi})$ assuming the isothermal DM halo model [32,33] with a local dark matter density of 0.3 $\mathrm{GeV}/c^2/\mathrm{cm}^3$, a circular velocity of 220 km/s, a galactic escape velocity of 544 km/s, and an average Earth velocity of 245 km/s. $P_{\mathrm{DM}}(\mathrm{S1}^i,\mathrm{S2}^i)$ and $P_{nbkg}(\mathrm{S1}^i,\mathrm{S2}^i)$ are the probability distribution functions (PDFs) of NR recoil signals for a WIMP with given mass and neutron background, respectively, obtained using the NEST-based MC simulation employing the PDE, EEE, and SEG described earlier. $\epsilon_{\mathrm{NR}}(\mathrm{S1}^i,\mathrm{S2}^i)$ is the NR detection efficiency from Fig. 6, with acceptance set to zero if S1 and S2 are outside the ranges of (2,30) and (300,10 000) PEs. To obtain the expected measured dark matter and neutron background events, the NR efficiency function has to be averaged over the expected dark matter or neutron background PDF [$\langle\epsilon_{\mathrm{NR}}\rangle_{\mathrm{DM}}$ and $\langle\epsilon_{\mathrm{NR}}\rangle_{nbkg}$ in Eq. (4)]. $N_{\mathrm{ER}}$ and $N_{\mathrm{Acc}}$ are the total number of ER and accidental background with detection efficiency taken into account, and $P_{\mathrm{ER}}(\mathrm{S1}^i,\mathrm{S2}^i)$ [taken to be the same as that obtained from ER calibration from Fig. 7(a), supported by the MC] and $P_{\mathrm{Acc}}(\mathrm{S1}^i,\mathrm{S2}^i)$ [from Fig. 8(c)] are the corresponding PDFs. The contamination of the accidental background in the ER calibration run is neglected due to the dominating ER rate in the calibration runs. The expected background events are taken from the top row of Table IV. To allow systematic variation in the global efficiency, four normalization nuisance parameters ($\delta_{\mathrm{DM}}$, $\delta_{\mathrm{ER}}$, $\delta_{\mathrm{Acc}}$ and

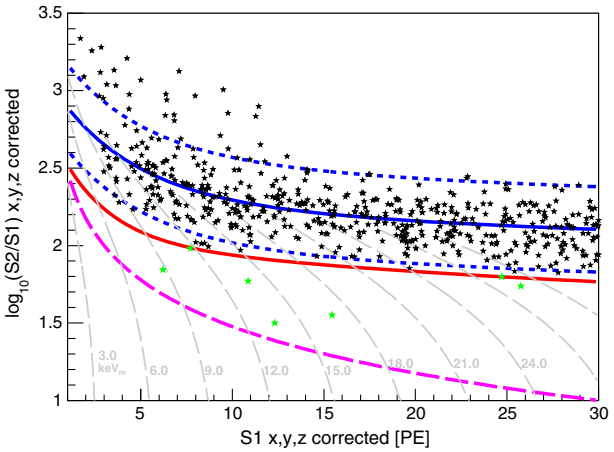


FIG. 10 (color online). The band of $\log_{10}(\mathrm{S2/S1})$ vs S1 for the dark matter search data. The ER band is indicated by the blue solid line (median) and the dashed line ($\pm 2\sigma$). The median of the NR band is indicated as the solid red line. The dashed magenta line is the 300 PE cut on S2. The green stars represent events below the NR median. The gray dashed lines are the equal-energy lines with NR energy indicated in the figures.

TABLE IV. The expected and measured events (in units of events) in 80.1 live-day dark matter search data.

| | ER | Accidental | Neutron | Total expected | Total observed |
|---|---|---|---|---|---|
| All | 503.7 | 35.1 | 0.35 | 539.1 | 542 |
| Below NR med | 2.5 | 4.2 | 0.18 | 6.9 | 7 |

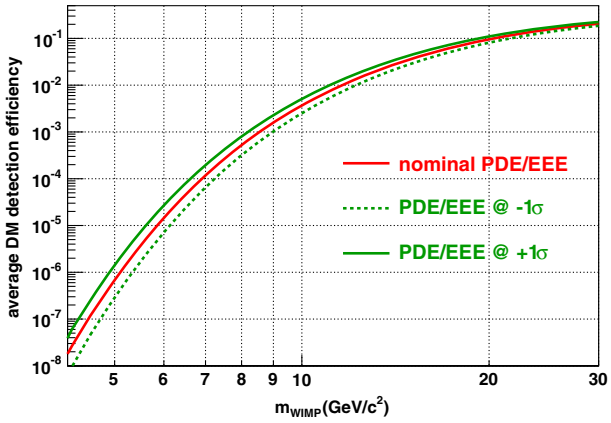


FIG. 11 (color online). The overall detection efficiency for WIMPs at different masses (red) and those obtained with PDE and EEE set at $+1\sigma$ (solid green) and $-1\sigma$ (dashed green).

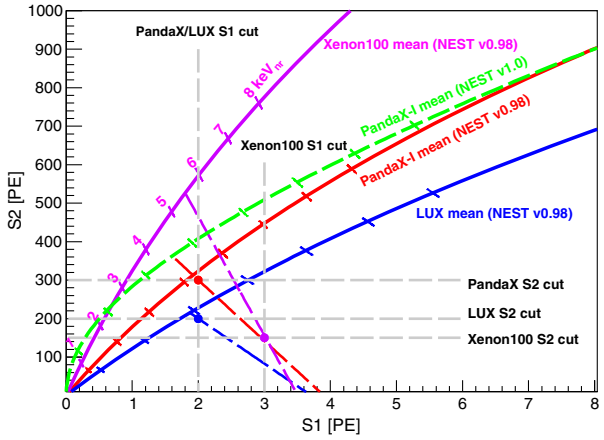


FIG. 12 (color online). The comparison of the mean energy thresholds, translated from the cuts on S1 and S2, for different experiments under the same energy model (NEST v0.98). The solid curves (red: PandaX; violet: XENON100; blue: LUX) represent the mean values for S1 and S2 obtained from NEST with slanted ticks (along the equal-energy vector) indicating the corresponding mean NR energy in divisions of $\mathrm{keV}_{nr}$. The curve for PandaX based on NEXT v1.0 is drawn as the green dashed curve. The selection thresholds in S1 and S2 are indicated in the figure as the solid circles. The antidiagonal dashed lines (red: PandaX; violet: XENON100; blue: LUX) are the equal-energy lines projected from the corresponding threshold points for different experiments.

$\delta_{nbkg}$) are included for the four types of events, constrained by Gaussian variations [$G$'s in Eq. (3)] of 20% (DM), 15% (ER), 10% (accidental) and 50% (neutron background) in the penalty terms [34,35].

The average WIMP detection efficiency $\langle \epsilon_{\mathrm{NR}} \rangle_{\mathrm{DM}}$, obtained by combining the NR efficiency with the WIMP PDF (with fluctuations in S1 and S2 properly taken into account), strongly depends on the WIMP mass, which is depicted in Fig. 11. The lower the WIMP mass, the softer the recoil energy distribution, and therefore the selection threshold on S1 and S2 would more strongly suppress the overall efficiency. To compare the effects of selection thresholds of different experiments on the NR energy, the mean NR energy curves in S1 and S2 are plotted in Fig. 12 based on the NEST-0.98 model with the PDE, EEE, and SEG values from PandaX, XENON100 [36], and LUX [12]. Our selection threshold is at about 4.2 $\mathrm{keV}_{nr}$ in both S1 and S2. XENON100 achieved an S2 threshold of less than 2 $\mathrm{keV}_{nr}$ but a much higher S1 threshold of about 8 $\mathrm{keV}_{nr}$. LUX, on the other hand, achieved an average 3 $\mathrm{keV}_{nr}$ threshold on both S1 and S2, but in Ref. [12] they chose to drop the NR efficiency entirely below 3 $\mathrm{keV}_{nr}$. The NEST-1.0 model predicts a higher charge yield for NR, in which case our S1 threshold would stay, but the S2 threshold would improve to about 2.8 $\mathrm{keV}_{nr}$, leading to a better sensitivity for low-mass WIMPs. Nevertheless, we chose the NEST-0.98 model to report our final WIMP results.

The best-fit value to maximize the likelihood function is found at $m_\chi = 27.5\ \mathrm{GeV/c^2}$ with a $\sigma_{\chi,N}$ at $4.1 \times 10^{-45}\ \mathrm{cm^2}$. The value of the likelihood is also consistent with that from the null hypothesis within $1\sigma$, indicating no significant excess over the background. To set the WIMP search upper limit, a standard profile likelihood ratio statistic is formed [34,35]. A Feldman and Cousin approach [37] is used to fit the data as well as a large number of MC simulations using the signal hypothesis at each grid point of $(m_\chi, \sigma_{n-\chi})$. The 90% C.L. upper limit obtained with this approach is shown in Fig. 13 together with the world data, and is verified to be very similar to that obtained assuming an approximate half-$\chi^2$ distribution of the test statistic [34]. A binned likelihood method developed in the independent analysis yields an upper limit in good agreement with the above. The upper limit excludes a WIMP mass of 10 $\mathrm{GeV/c^2}$ down to a cross section of $1.41 \times 10^{-43}\ \mathrm{cm^2}$, and the lowest excluded cross section is $1.01 \times 10^{-44}\ \mathrm{cm^2}$ at a WIMP mass of 44.7 $\mathrm{GeV/c^2}$. Under the elastic, spin-independent, and isospin-conserving WIMP-nucleon scattering model, our limits strongly disfavor the WIMP interpretation of the results from DAMA/LIBRA, CoGeNT, CDMS-II-Si and CRESST-II. It is noteworthy that the PDE and EEE used in this analysis are conservative in nature since we inhibited the unstable PMTs. In addition, we have considered the average WIMP detection efficiency with WIMP mass dependence in this analysis (Fig. 11). Compared to that in Ref. [13], in which the DM efficiency was treated only as a function of S1, this treatment is more realistic. Even with these realistic treatments, our results still set a stringent limit at the low-WIMP-mass region, with a tighter bound than SuperCDMS above a WIMP mass of 7 $\mathrm{GeV/c^2}$, and the best reported bound in a dual-phase xenon detector below a WIMP mass of 5.5 $\mathrm{GeV/c^2}$. Note that one of the key differences between this analysis and that from LUX in Ref. [12] is that the latter made a conservative choice to model no

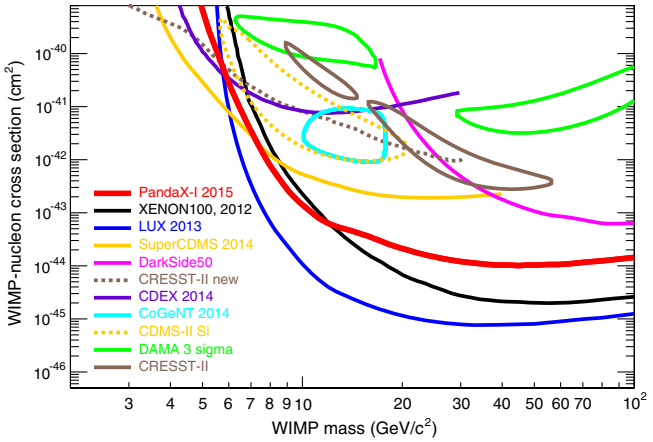


FIG. 13 (color online). The 90% C.L. upper limit for the spin-independent isoscalar WIMP-nucleon cross section for the PandaX-I experiment (red curves). Recent world results are plotted for comparison: XENON100 225 day results [11] (black solid), LUX first results [12] (blue), SuperCDMS results [15] (orange solid), DarkSide results [14] (magenta solid), CRESST-II 2014 limits [8] (brown dashed), and CDEX 2014 limits [17] (solid violet). The claimed WIMP signals are shown as closed contours: CoGeNT 2014 results [6] (cyan solid), CDMS-II-Si results [9] (gold dashed), DAMA/LIBRA $3\sigma$ contours [38] (green solid), and CRESST-II 2012 results [7] (brown solid).

signal generation for events below 3 keV$_{nr}$, while in our treatment the signal generation is continuous to zero energy and therefore low-energy events below the mean energy threshold of 4.2 keV$_{nr}$ could still fluctuate upwards into the detection region.

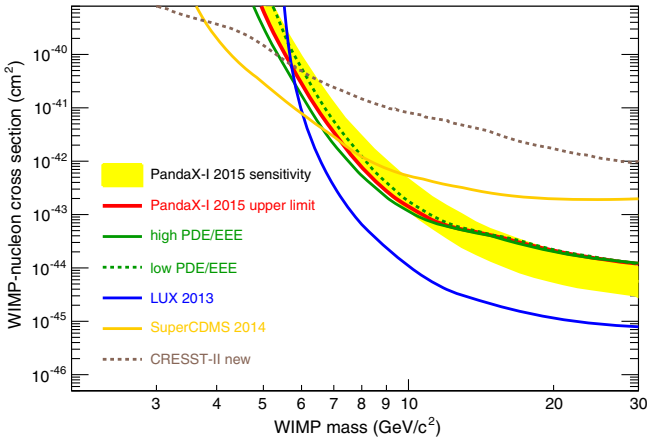


FIG. 14 (color online). PandaX-I WIMP search limit from the data (red line) overlaid with the $\pm 1\sigma$ sensitivity band obtained from toy MC (yellow) as well as the alternative upper limits using either $+1\sigma$ or $-1\sigma$ values for the PDE and EEE, but with the same NEST-0.98 model. For comparison, a few world leading limits for the low-mass WIMP are plotted: LUX first results [12] (blue), SuperCDMS results [15] (orange), and CRESST-II 2014 limits [8] (brown dashed).

The experimental sensitivity band is obtained using the same approach as above but with hundreds of 80.1-day background-only toy MCs based on Table IV using a prescribed PDF for each event type, from which one obtains a distribution of "upper limits." In Fig. 14, our upper limit is overlaid with the $\pm 1$-$\sigma$ sensitivity band. Consistency is observed, confirming no significant excess over background.

To study shape-related systematic uncertainties separately,[4] we performed calculations of upper limits by setting both PDE and EEE at either $+1\sigma$ or $-1\sigma$. The resulting limits are overlaid in Fig. 14. As expected, the higher efficiency would lead to tighter bounds in the low-mass region and vice versa. The (more aggressive) upper limit obtained with dark matter PDFs generated from the NEST-1.0 model is very close to that with the $+1\sigma$ PDE/EEE. These are sizable influences but are comparable with the sensitivity band, and therefore they do not change the main conclusion of our results.

## VIII. CONCLUSION AND OUTLOOK

In summary, we reported the low-energy dark matter search results with the $54.0 \times 80.1$ kg-day full exposure of the PandaX-I experiment. In this analysis, compared to the first results, we made a number of improvements in signal identification, background classification and rate and shape estimates, a realistic treatment on the efficiency for very low-recoil-energy events, as well as profile likelihood ratio fits to obtain the final WIMP search limit. Observing no significant excess over background, our results strongly disfavor the WIMP interpretation of the results from DAMA/LIBRA, CoGeNT, CDMS-II-Si and CRESST-II. Our bound is tighter than that from SuperCDMS above a WIMP mass of 7 GeV$/c^2$, and is the lowest reported limit below a WIMP mass of 5.5 GeV$/c^2$ in xenon dark matter experiments to date, showing that liquid xenon detectors can be competitive for low-mass WIMP searches.

The results from PandaX-I are crucial in guiding the future development of the PandaX program. The second-phase experiment, PandaX-II, constructed with a liquid xenon target of 500 kg sensitive mass and lower background materials for the cryostat and TPC, is under preparation at CJPL. The PandaX-II detector is expected to improve both on the light and charge collection efficiency and push the dark matter sensitivity beyond the current best reach in a wide range of WIMP masses.

[4]The shape systematics could also be introduced into the fitter via nuisance parameters. However, to explicitly show the size of the effects and to simplify the fitter computation, we chose to apply these systematic variations "by hand."

## ACKNOWLEDGMENTS

This project has been supported by a 985-III grant from Shanghai Jiao Tong University, a 973 grant from the Ministry of Science and Technology of China (Grant No. 2010CB833005), grants from the National Science Foundation of China (Grants No. 11055003 and No. 11435008), and a grant from the Office of Science and Technology in Shanghai Municipal Government (Grant No. 11DZ2260700). This work is supported in part by the CAS Center for Excellence in Particle Physics (CCEPP). X. C. acknowledges support from China Postdoctoral Science Foundation Grant 2014M551395. The project has also been sponsored by Shandong University, Peking University, the University of Maryland, and the University of Michigan. We would like to thank many people including Elena Aprile, Xianfeng Chen, Carter Hall, T. D. Lee, Zhongqin Lin, Chuan Liu, Lv Lv, Yinghong Peng, Weilian Tong, Hanguo Wang, James White, Yueliang Wu, Qinghao Ye, Qian Yue, and Haiying Zhao for help and discussion at various levels. We are particularly indebted to Jie Zhang for his strong support and crucial help during many stages of this project. Finally, we thank the following organizations and personnel for indispensable logistics and other support: the CJPL administration including directors Jianping Cheng and Kejun Kang and manager Jianmin Li, Yalong River Hydropower Development Company Ltd. including the chairman of the board Huisheng Wang, and manager Xiantao Chen and his JinPing tunnel management team from the 21st Bureau of the China Railway Construction Co.

[1] See for example, G. Bertone, D. Hooper, and J. Silk, Phys. Rep. **405**, 279 (2005).
[2] See for example, R. R. Volkas and K. Petraki, Int. J. Mod. Phys. A **28**, 1330028 (2013), K. M. Zurek, Phys. Rep. **537**, 91 (2014), and the references therein.
[3] See, e.g. G. Jungman, M. Kamionkowski, and K. Griest, Phys. Rep. **267**, 195 (1996), and the reference therein.
[4] D. Akimov, Nucl. Instrum. Methods Phys. Res., Sect. A **628**, 50 (2011); R. Gaitskell, Annu. Rev. Nucl. Part. Sci. **54**, 315 (2004). For more recent experiments, see talks at the 2014 Dark Matter Conference at UCLA, https://hepconf.physics.ucla.edu/dm14/agenda.html.
[5] R. Bernabei *et al.* (DAMA Collaboration), Eur. Phys. J. C **56**, 333 (2008), **67**, 39 (2010), **73**, 2648 (2013).
[6] C. E. Aalseth *et al.* (CoGeNT Collaboration), Phys. Rev. Lett. **106**, 131301 (2011), Phys. Rev. D **88**, 012002 (2013), and latest analysis using maximum likelihood method in arXiv:1401.6234.
[7] G. Angloher *et al.* (CRESST Collaboration), Eur. Phys. J. C **72**, 1971 (2012).
[8] G. Angloher *et al.* (CRESST Collaboration), Eur. Phys. J. C **74**, 3184 (2014).
[9] R. Agnese *et al.* (CDMS Collaboration), Phys. Rev. Lett. **111**, 251301 (2013).
[10] D. Y. Akimov *et al.* (ZEPLIN-III Collaboration), Phys. Lett. B **709**, 14 (2012).
[11] E. Aprile *et al.* (XENON100 Collaboration), Phys. Rev. Lett. **109**, 181301 (2012).
[12] D. S. Arkerib *et al.* (LUX Collaboration), Phys. Rev. Lett. **112**, 091303 (2014).
[13] M. J. Xiao *et al.* (PandaX Collaboration), Sci. China Phys. Mech. Astron. **57**, 2024 (2014).
[14] P. Agnes *et al.* (DarkSide Collaboration), Phys. Lett. B **743**, 456 (2015).
[15] R. Agnese *et al.* (SuperCDMS Collaboration), Phys. Rev. Lett. **112**, 041302 (2014).
[16] R. Agnese *et al.* (SuperCDMS Collaboration), Phys. Rev. Lett. **112**, 241302 (2014).
[17] Q. Yue *et al.* (CDEX Collaboration), Phys. Rev. D **90**, 091701 (2014).
[18] S. C. Kim *et al.* (KIMS Collaboration), Phys. Rev. Lett. **108**, 181301 (2012).
[19] J. Angle *et al.* (XENON10 Collaboration), Phys. Rev. Lett. **107**, 051301 (2011); **110**, 249901(E) (2013).
[20] M. SzydagisM Szydagis, N. Barry, K. Kazkaz, J. Mock, D. Stolp, M. Sweany, M. Tripathi, S. Uvarov, N. Walsh, and M Woods, J. Instrum. **6**, P10002 (2011).
[21] M. Szydagis, A. Fyhrie, D. Thorngren, and M. Tripathi, J. Instrum. **8**, C10003 (2013).
[22] B. Lenardo *et al.*, arXiv:1412.4417.
[23] W. Mu, X. Xiong, and X. Ji, Astropart. Phys. **61**, 56 (2015).
[24] X. Cao *et al.* (PandaX Collaboration), Sci. China Phys. Mech. Astron. **57**, 1476 (2014).
[25] K. J. Kang, J. P. Cheng, Y. H. Chen, Y. J. Li, M. B. Shen, S. Y. Wu, and Q. Yue, J. Phys. Conf. Ser. **203**, 012028 (2010); Q. Yue and H. T. Wong, J. Phys. Conf. Ser. **375**, 042061 (2012); J. Li, X. Ji, W. Haxton, and J. S. Y. Wang, Phys. Procedia **61**, 576 (2015); X. G. Cao *et al.*, Sci. China Phys. Mech. Astron. **57**, 1476 (2014).
[26] E. Aprile and T. Doke, Rev. Mod. Phys. **82**, 2053 (2010).
[27] Q. Lin, Ph.D. thesis, Shanghai Jiao Tong University, 2015 (to be published).
[28] Yoshino, Y. U. Spwada, and W. F. Schmidt, Phys. Rev. A **14**, 438 (1976).
[29] S. Agostinelli *et al.*, Nucl. Instrum. Methods Phys. Res., Sect. A **506**, 250 (2003); IEEE Trans. Nucl. Sci. **53**, 270 (2006).
[30] J. Angle *et al.* (XENON10 Collaboration), Phys. Rev. Lett. **100**, 021303 (2008).
[31] W. B. Wilson *et al.*, LANL technical note LA-13639-MS, 1999 (unpublished).
[32] M. C. Smith *et al.*, Mon. Not. R. Astron. Soc. **379**, 755 (2007).

[33] C. Savage, K. Freese, and P. Gondolo, Phys. Rev. D **74**, 043531 (2006).
[34] G. Cowan, K. Cranmer, E. Gross, and O. Vitells, Eur. Phys. J. C **71**, 1 (2011); **73**, 2501(E) (2013).
[35] E. Aprile *et al.* (XENON100 Collaboration), Phys. Rev. D **84**, 052003 (2011).
[36] E. Aprile *et al.* (XENON100 Collaboration), J. Phys. G **41**, 035201 (2014).
[37] G. J. Feldman and R. D. Cousins, Phys. Rev. D **57**, 3873 (1998).
[38] C. Savage, G. Gelmini, P. Gondolo, and K. Freese, J. Cosmol. Astropart. Phys. 04 (2009) 010.